



Two-dimensional island dynamics: Role of step energy anisotropy

S. Kodambaka^{a,*}, S.V. Khare^b, I. Petrov^a, J.E. Greene^a

^a *Department of Materials Science and the Frederick Seitz Materials Research Laboratory, University of Illinois,
104 South Goodwin Avenue, Urbana, IL 61801, USA*

^b *Department of Physics and Astronomy, University of Toledo, Toledo, OH 43606, USA*

Accepted 12 October 2005

Available online 6 December 2005

Abstract

Studies of surface dynamics, including the kinetics of two-dimensional (2D) island coarsening/decay, shape fluctuations, and shape evolution, enable determination of the rate-limiting mechanisms, corresponding surface mass transport parameters, and step energies. Most models describing these phenomena assume isotropic (circular) or near-isotropic island shapes and, hence, isotropic step energies. However, even simple elemental metal surfaces are anisotropic and more complex compound surfaces such as the low-index planes of TiN, GaAs, GaN, ZnO, Al₂O₃, ZrO₂, are highly anisotropic. Here, we describe recent progress toward developing generalized theoretical and experimental approaches, applicable for analyses of 2D island coarsening/decay kinetics, coalescence kinetics, and determination of orientation-dependent step energies and step stiffnesses, on both isotropic and highly anisotropic surfaces.

© 2005 Elsevier B.V. All rights reserved.

Contents

1. Introduction.....	56
2. Absolute orientation-dependent step energies	57
2.1. Equilibrium island shape analyses	58

Abbreviations: AES, Auger electron spectroscopy; AFM, atomic force microscopy; ECS, Equilibrium crystal shape; FIM, field ion microscopy; LEEM, low-energy electron microscopy; LEED, low-energy electron diffraction; PEEM, photo-emission electron microscopy; STM, scanning tunneling microscopy; TEM, transmission electron microscopy; 2D, two dimensional; 3D, three dimensional; UV, ultra violet; GT, Gibbs Thomson.

* Corresponding author. Tel.: +1 217 333 3481; fax: +1 217 244 1638.

E-mail address: kodambak@uiuc.edu (S. Kodambaka).

2.1.1. Effect of surface stress on 2D equilibrium island shapes.....	62
2.2. Anisotropic 2D island shape fluctuation analyses	64
3. Analyses of 2D island decay (Ostwald ripening) kinetics	67
3.1. Modified Gibbs–Thomson relation for anisotropic islands.....	69
4. Anisotropic 2D island coalescence kinetics	70
5. Conclusions.....	73
Acknowledgements	74
References	74

1. Introduction

Thin film growth is a complex phenomenon controlled by the interplay of both thermodynamic and kinetic driving forces. Fundamental understanding of the processes governing microstructural and morphological evolution of thin film surfaces can be developed via studies of the dynamics of surfaces at the atomic scale. Prior to the invention of STM [1] and related scanning probe microscopy tools such as AFM [2], FIM [3] was the only real-space imaging technique available for resolving individual atoms on surfaces and for studying dynamic processes such as surface diffusion of single adatoms and small 2D islands [4,5]. Despite the restrictions on the type and size of materials that can be used for FIM studies, which require use of high electrical fields and sharp single-crystalline tips, detailed investigations of adatom transport mechanisms have been carried out on a wide variety of metal surfaces [6].

The advent of high-speed variable-temperature and -pressure STM allows studies of surface dynamics at video rates [7–11] for a wider range of materials. Using STM, in situ studies of the diffusion of adspecies (adatoms and advacancies), kinks, steps, and 2D islands [12–21] are carried out over a wide range of temperatures (20–1500 K). From analyses of the changes in successive images, atomic processes contributing to these phenomena are quantified. The kinetics of nucleation and growth [22–24] on crystalline surfaces are routinely studied in situ, either in ultra-high vacuum or electrolytic environments. A related tool, the AFM, is also used to study the nucleation and growth kinetics of crystals in liquid environments [25,26].

LEEM [27] is another surface-sensitive technique (complementary to STM) in which a coherent, low-energy electron beam (typically 1–100 eV) illuminates the sample; the electrons undergo diffraction and are captured by an objective lens to form a real-space image of the surface. Using a contrast aperture, diffracted beams corresponding to either (0,0) or fractional order spots are selected to yield bright-field or dark-field images, respectively. In LEEM, single-atom-height steps on the surface can be resolved by phase contrast. Surface lateral resolution is typically of the order of several tens of Ångströms. Diffraction and chemical contrast also provide information about the surface. Since LEEM is not a scanning microscope, images are acquired at video rates, thus providing sufficient time resolution for real-time studies of dynamic phenomena such as epitaxy, interface formation, and surface morphological evolution on large lateral length scales (1–10 μm) over a wide range of temperatures. LEEM, best suited for investigating electrically conducting crystalline samples, has been used to study surface diffusion of 2D metal islands [28], surface phase transformations [29], alloy formation, step fluctuation kinetics, interlayer mass transport, and bulk diffusion. PEEM is a related technique, in which photo-electrons generated by an incident UV or an X-ray light source (rather than an electron gun) are used for imaging. PEEM has proven to be an effective tool for following chemical reactions on catalytic surfaces [30].

There are several excellent review articles covering different aspects of atomic-scale dynamics of the early stages of thin film growth. Zinke-Allmann and co-workers [31,32] summarized the theoretical and experimental understanding of cluster formation phenomena in general, while focusing on the role of adatom surface diffusion and binding energies on cluster formation kinetics. Tromp and Hannon [33] described methods for quantitative analyses of nucleation and growth processes on surfaces. The reviews by Jeong and Williams [34] and Giesen [35] provide theoretical background and describe experimental and computational techniques for investigating and characterizing the dynamics of metastable structures on surfaces, determining step energetics and mass transport parameters, and hence developing an atomic-scale understanding of the stability of solid/vacuum and solid/liquid interfaces. Recently, Bonzel and co-workers [36–38] reviewed new experimental methods for analyses of temperature-dependent 3D equilibrium crystal shapes and 2D islands as a means to extract absolute surface, step, and kink formation energies.

All of the above reviews assume isotropic (circular) or near-isotropic step energies. However, even simple elemental metal surfaces are anisotropic and more complex compound surfaces such as the low-index planes of TiN, GaAs, GaN, ZnO, Al₂O₃, ZrO₂, are highly anisotropic. Here, we describe recent progress toward developing generalized theoretical and experimental approaches for elucidating the effects of step edge energy anisotropy on 2D island dynamics. We focus on the kinetics of 2D island coarsening/decay (Ostwald ripening), temporal fluctuations around equilibrium island shapes, shape relaxation following island coalescence in anisotropic systems, and the effect of intrinsic surface stress anisotropy on island shapes. Section 2 describes methods to determine absolute step energies as a function of step orientation, while Sections 3 and 4 discuss theoretical analyses of 2D island coarsening/decay and coalescence kinetics, respectively. Conclusions and future prospects in this area are discussed in Section 5.

2. Absolute orientation-dependent step energies

The step formation energy per unit length β is the 2D analog of the surface free energy per unit area γ , a fundamental parameter used to describe crystals. Just as $\gamma(\hat{\mathbf{n}})$, where $\hat{\mathbf{n}}$ is a unit vector normal representing a facet orientation, determines the 3D ECS, $\beta(\varphi)$ determines the 2D equilibrium island shape. φ is defined as the local normal to the equilibrium shape R at θ . A related property, the step-edge stiffness $\tilde{\beta}(\varphi)$, defined as

$$\tilde{\beta}(\varphi) \equiv \beta(\varphi) + d_{\varphi\varphi}\beta(\varphi), \quad (1)$$

is proportional to the island chemical potential, and hence controls island coarsening/decay and shape-evolution kinetics. For convenience, we use the notation d_{φ} and $d_{\varphi\varphi}$ to represent $d/d\varphi$ and $d^2/d\varphi^2$, respectively, in Eq. (1) and in following sections.

Absolute step energy β and stiffness $\tilde{\beta}$ values for selected orientations have been determined from equilibrium step distributions on vicinal surfaces [39], step fluctuation measurements [40], 3D ECSs [41–43,160,161], and the temperature-dependence of 2D equilibrium island shapes [44–46, 162]. Orientation-averaged β values have been extracted from 2D island decay [47–49] and near-isotropic island shape fluctuation measurements [50,51]. Reviews by Bonzel [36,37], Jeong and Williams [34], Giesen [35], and Zandvliet [52,53], for Si(001) and Ge(001) in particular, summarize available methods for the determination of either orientation-averaged step energetics or step and surface energies

for a particular orientation. Extraction of $\beta(\varphi)$ using these approaches requires additional experiments. Therefore, we focus only on recently developed methods for direct determination of absolute orientation-dependent step energies and step stiffnesses from a single experiment.

In the following sections, we describe analyses of equilibrium anisotropic island shapes, in combination with time-dependent shape fluctuations, as a means to obtain absolute φ -dependent step energies and stiffnesses.

2.1. Equilibrium island shape analyses

The well-known Wulff construction provides a method for determining the 3D ECS from the Wulff plot. Fig. 1 is a geometric representation of the Wulff and inverse-Wulff construction procedures for an arbitrary equilibrium crystal shape $W(x_1, x_2, x_3) = 0$. Geometrically, construction of a Wulff plot involves drawing planes perpendicular to normal unit vectors at every point on the surface free energy graph $\gamma(\hat{\mathbf{n}})$. The inner envelope of these planes corresponds to the equilibrium crystal shape (solid line in Fig. 1). Similarly, the “inverse” Wulff construction allows a determination of $\gamma(\hat{\mathbf{n}})$ from the ECS by drawing normal vectors (short dashed line) to the tangent planes (dashed line) along the crystal boundary. The inner envelope of these normal vectors shown by the solid arrow in Fig. 1 yields *relative* values of $\gamma(\hat{\mathbf{n}})$. Mathematically, the equilibrium shape function is the Legendre transform of $\gamma(\hat{\mathbf{n}})$ and vice versa. Analytical expressions for the Wulff construction have been formulated in Cartesian coordinates [54–57]. For 2D islands, Nozières [57] derived an expression in polar coordinates relating β to the equilibrium shape and Khare et al. [58] provided analytical expressions of the Wulff theorem in generalized orthogonal coordinates. Specifically, in polar coordinates, the inverse Legendre transform of the 2D equilibrium island shape $R(\theta)$ yields *relative* values of $\beta(\varphi)$ through the relationship [57,58]

$$\beta(\varphi) = \lambda \frac{R(\theta)}{\left(1 + \left(\frac{\partial_\theta R(\theta)}{R(\theta)}\right)^2\right)^{1/2}}, \quad (2)$$

where φ is defined as

$$\varphi(\theta) = \theta - \arctan\left(\frac{\partial_\theta R(\theta)}{R(\theta)}\right) \quad (3)$$

and the symbol ∂ represents the partial derivative.

The proportionality constant λ in Eq. (2) is the equilibrium island chemical potential per unit area. Eqs. (2) and (3) offer an analytical approach for computing orientation-dependent $\beta(\varphi)$ values to within an orientation-independent constant λ . This method eliminates the conventional geometric construction of the inverse-Wulff plot, which involves the tedious procedure of drawing normal vectors from the center of mass of the island to the tangent lines at every point along $R(\theta)$, the envelope of which yields $\beta(\varphi)$. It is important to note that the equation $\beta_1/\beta_2 = R_1/R_2$, often referred to as the “Wulff relationship,” is *not* valid for any arbitrary facet/step orientations 1 and 2. The relationship is *only* valid for the orientations corresponding to maxima or minima in β , i.e. $\partial_\theta R(\theta) = 0$, as can be seen from Eqs. (2) and (3) which are applicable for the analysis of equilibrium shapes of 2D islands on flat terraces and facets on 3D crystals. 2D islands are routinely observed on solid surfaces using surface imaging techniques such as LEEM and STM.

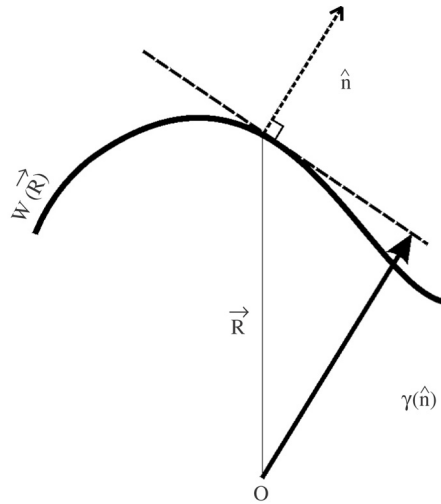


Fig. 1. Geometrical representation of the Wulff and inverse-Wulff plot constructions: at each point $\vec{R} = (x_1, x_2, x_3)$ on the equilibrium crystal shape defined by $W(x_1, x_2, x_3) = 0$, a plane is drawn tangential to the surface. The distance of the plane from the origin O is proportional to $\gamma(\hat{n})$, where γ is the surface energy of the plane with \hat{n} as the unit normal vector to the plane. Ref. [58].

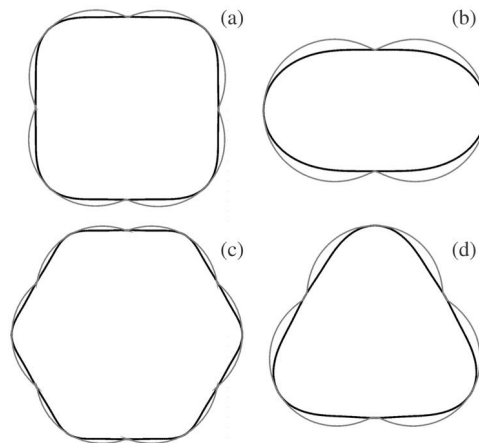


Fig. 2. Wulff plots, β versus φ , for commonly observed two-dimensional island shapes $R(\theta)$ on surfaces of cubic materials: (a) four-fold, (b) two-fold, (c) six-fold, and (d) three-fold symmetric island shapes. The black curves represent the equilibrium island shape functions $R(\theta)$, while the grey curves correspond to $\beta(\varphi)$ obtained analytically using Eqs. (2) and (3) with λ set to unity. Ref. [58].

Fig. 2(a)–(d) are polar plots $R(\theta)$ of rectangular, triangular, square, and hexagonal islands on 2-, 3-, 4-, and 6-fold symmetric surfaces, respectively. For an n -fold symmetric surface, island shapes are obtained using simple functions of the form $R(\theta) \equiv a + b \cdot \sin(n\theta)$, with $n = 2, 3, 4$, or 6 . From $R(\theta)$, relative values of $\beta(\varphi)$ can be derived using Eqs. (2) and (3). The light grey curves in Fig. 2 are plots of calculated $\beta(\varphi)$ data obtained with $\lambda = 1$.

From Eqs. (2) and (3), it can be shown that $\tilde{\beta}(\varphi)$ is related to the curvature $\kappa(\theta)$ of the equilibrium shape $R(\theta)$ through the expression [58,59]

$$\tilde{\beta}(\varphi) = \frac{\lambda}{\kappa(\theta)} \quad (4)$$

with

$$\kappa(\theta) = \frac{R^2 + 2(\partial_\theta R)^2 - R\partial_{\theta\theta} R}{[R^2 + (\partial_\theta R)^2]^{3/2}}. \quad (5)$$

Also, from Eqs. (2) and (3), Khare et al. [58] derived the relationship $\partial_\varphi \beta / \beta(\varphi) = \partial_\theta R / R(\theta)$ and used this together with the inverse transforms:

$$R(\theta) = \left(\frac{1}{\lambda}\right) \sqrt{\beta^2(\varphi) + (\partial_\varphi \beta)^2} \quad (6)$$

and

$$\theta = \varphi + \arctan(\partial_\varphi \beta / \beta(\varphi)) \quad (7)$$

to predict island equilibrium shapes from $\beta(\varphi)$. In the absence of prior knowledge of $\beta(\varphi)$, a microscopic approach such as the Ising model [60–66] can be used to calculate $\beta(\varphi)$ or equilibrium island shapes directly [67,68].

The procedures described thus far, which are general and valid for any material system, can be used to analytically determine the *relative* orientation dependence of β from $R(\theta)$, and vice versa. Fig. 3 shows two sets of consecutive STM images of 2D TiN vacancy islands on atomically smooth TiN(001) (Fig. 3(a)) and (111) (Fig. 3(b)) terraces at 1140 K and 1200 K, respectively [69–71]. The observed fluctuations in island shapes $r(\theta, t)$ are due to thermally induced random motion of the diffusing species. Equilibrium island shapes $R(\theta)$, defined as $R(\theta) \equiv \langle r(\theta, t) \rangle$, for the TiN(001) and TiN(111) islands corresponding to Figs. 3(a) and (b) are plotted as open symbols in the upper and lower panels of Fig. 4(a). The solid lines are analytic fits obtained with Lorentzian functions of general form, $R = R_o + \frac{a}{[1+b(\theta-\theta_c)^2]}$, where R_o , a , b , and θ_c are fitting parameters. From $R(\theta)$, relative values of $\beta(\varphi)$ can be derived using Eqs. (2) and (3).

Polar plots of $\beta(\varphi)$ (dotted line) calculated with $\lambda = 1$ for TiN(001) and TiN(111) islands in Figs. 3(a) and (b) are shown in the upper and lower panels, respectively, of Fig. 4(b). The straight and corner steps are $\langle 110 \rangle$ and $\langle 100 \rangle$ for TiN(001) islands, and $\langle 110 \rangle$ steps with different local symmetry, labeled S_1 and S_2 , for TiN(111) islands. These $\langle 110 \rangle$ steps on NaCl-structure TiN(111) form $\{100\}$ and $\{110\}$ nanofacets with respect to the terrace, analogous to the $\{111\}$ and $\{100\}$ nanofacets formed by the alternating $\langle 110 \rangle$ steps bounding a simple face centered cubic (111) surface.

The relations given above are, however, based upon the assumptions that the island shape is independent of island size and that the functions $R(\theta)$ and $\beta(\varphi)$ are symmetric about the island's center of mass. These assumptions may not be valid for surfaces exhibiting either anisotropic surface stress or reconstruction [72–74]. Fig. 5 is an illustration of a typical $\langle 110 \rangle$ surface of a face-centered cubic material, for example Au(110), Pt(110), etc., which undergoes a missing row reconstruction and thus exhibits broken mirror symmetry. In the case of Au(110), Frenken and co-workers [75–79] found that 2D equilibrium island shapes are symmetric about their centers of mass, i.e. $R(2\pi/n - \theta) = R(\theta)$ for an island with an n -fold symmetry. However, the island's center of mass does not coincide with the point of

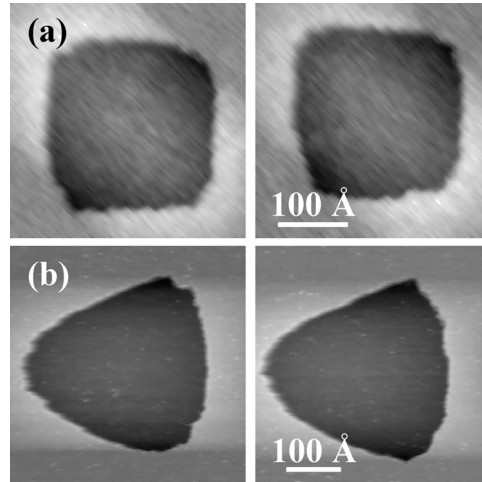


Fig. 3. Consecutive STM images of 2D TiN vacancy islands on atomically smooth (001) and (111) TiN terraces, respectively. Image size, scan rate, and annealing temperature T_a : (a) $338 \times 338 \text{ \AA}^2$, 15 s/frame, and 1140 K; (b) $430 \times 430 \text{ \AA}^2$, 32 s/frame, and 1200 K. The images are taken from Refs. [69] and [71].

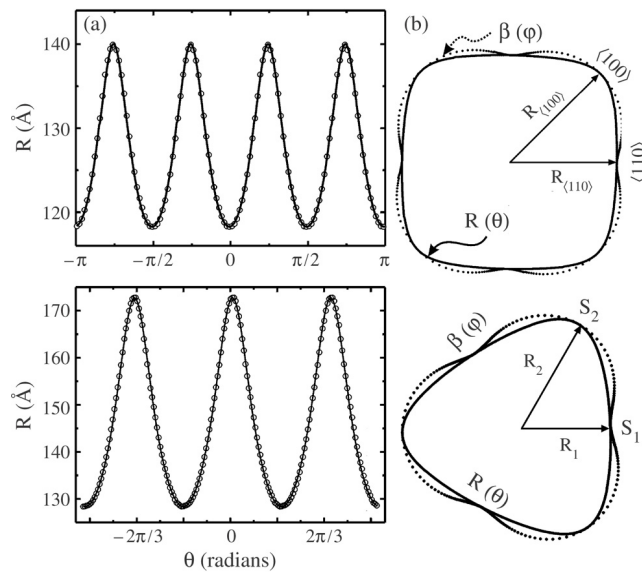


Fig. 4. Upper panel: (a) plot of R versus θ for the TiN(001) island shown in Fig. 3(a), and (b) polar plot of R versus θ and β versus φ determined using Eqs. (2) and (3) with $\lambda = 1$. Lower panel: The corresponding plots for the TiN(111) island in Fig. 3(b). The two $\langle 110 \rangle$ close-packed steps bounding the TiN(111) island are labeled S_1 and S_2 , while the corresponding radial distances from the center of the island are R_1 and R_2 , respectively. Open circles represent experimental data and the solid lines are the analytical fits obtained using Lorentzian functions of general form $R = R_o + \frac{a}{[1+b(\theta-\theta_c)^2]}$. Refs. [69] and [71].

origin for the Wulff plot [80]. That is, $\beta[(2\pi/n)-\varphi] \neq \beta(\varphi)$. Rather, $\beta[(2\pi/n)-\varphi] = \beta(\varphi) + 2d \cos(\varphi)$, where d is the distance between the island's center of mass and the Wulff point [77]. Fig. 6 shows the equilibrium shape of the island and its Wulff point.

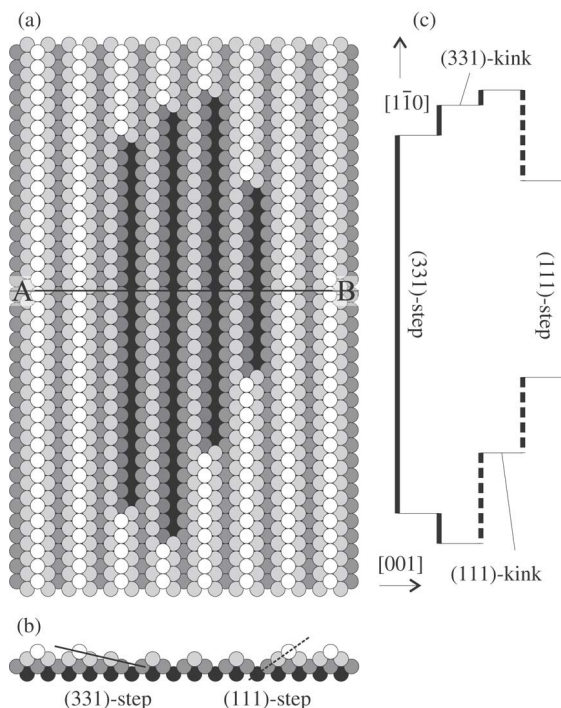


Fig. 5. (a) Schematic diagram showing a vacancy island in the (1×2) reconstructed Au (110) surface. (b) Cross section along AB. As a consequence of the missing-row reconstruction inside and outside the vacancy island, the steps at the left and right sides of the vacancy island are different. (c) Schematic top view of the island contour. The (331) steps are indicated with solid lines and the (111) steps with dashed lines. Ref. [78].

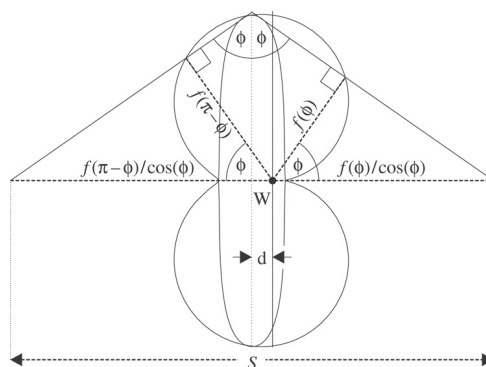


Fig. 6. Wulff construction for an island on a Au (110) 2×1 surface. As derived in the text, when the condition $\beta(2\pi/n - \varphi) = \beta(\varphi) + 2d \cos(\varphi)$ is satisfied for all angles φ , the shape of the island is mirror symmetric with respect to a symmetry axis at a distance d from the Wulff point W. Ref. [78].

2.1.1. Effect of surface stress on 2D equilibrium island shapes

So far, we have discussed the case in which 2D island shapes are determined only by the step energy anisotropy [58] and elastic stress does not play a role. However, as pointed out by Vilfan [81], for

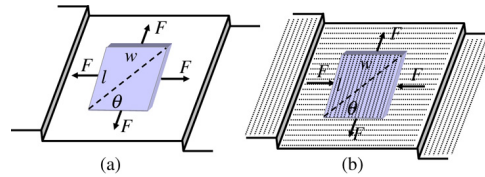


Fig. 7. Schematic representations of (a) heteroepitaxial and (b) homoepitaxial 2D rectangular-shaped islands with length l and width w grown on a surface exhibiting twofold symmetry. F represents the elastic force monopole along the island periphery induced by the lattice mismatch between the island and substrate in Fig. 7(a), and by the intrinsic surface stress anisotropy in Fig. 7(b). Dashed lines indicate alternating stress domains arising from surface stress anisotropy. Note that the force monopoles on the two l sides in Fig. 7(b) point in a direction that is opposite to the force monopole in Fig. 7(a). Adapted from Ref. [72].

islands on (110) reconstructed face centered cubic metal surfaces, such as Ag and Au, elastic step–step interactions can affect 2D island shapes. Carlon and van Beijeren [82] predicted that 2D islands on reconstructed fcc(110) metal surfaces exhibit “almond” shapes. Frenken and coworkers [75,79] carried out a detailed study of the decay of such almond-shaped islands on Au (110) and found that the decay behavior of 2D islands cannot be predicted by classical mean-field theory [83]. They attributed this to the highly anisotropic shapes of the islands [75,76,79].

Surface reconstruction can cause anisotropic stress on homoepitaxial islands. Consider, for example, the (2×1) reconstructed surfaces of Si(001) and Ge(001). The reconstruction induces surface stress in which domains on adjacent terraces are oriented perpendicular to each other. The surface stress is highly anisotropic and is tensile along the dimer bond and compressive along the dimer row [84–89]. Such a surface with a broken orientational symmetry and an intrinsic surface stress tensor leads to the spontaneous formation of elastic-stress domains [84–86]. A variety of interesting 2D and 3D surface morphological patterns can form due to interactions between such domains [84–86,90,91]. This intrinsic surface stress anisotropy also leads to the formation of elastic force monopoles at the 2D island edges, as shown for 2D rectangular-shaped islands on Si(001) in Fig. 7 [72]. The magnitude of these monopoles is proportional to the misfit strain and the surface step height and causes even homoepitaxial islands to have anisotropic shapes [72]. The effect of these forces on the equilibrium shape of hetero- and homoepitaxial islands was investigated theoretically by Li et al. [72] using continuum elasticity theory. They showed that, in the presence of such intrinsic stress anisotropy, island shapes depend not only on the orientation dependence of the step energies, but also on the anisotropy of the surface stress.

The theoretical ideas presented in Ref. [72] were applied to analyze size-dependent changes in the shapes of 2D Si(001) [92] and Ge(001) [93] islands. From the temperature- and size-dependence of the island shapes, absolute step energies and intrinsic surface stress anisotropies were measured. For Si(001), the surface stress anisotropy was found to be $68 \pm 3 \text{ meV}/\text{\AA}^2$ at $T = 1128 \text{ K}$ and $80 \pm 4 \text{ meV}/\text{\AA}^2$ at 968 K [92]. These results are in good agreement with calculated values for Si(001) obtained using first principles [94–96]. For Ge(001), Middel et al. [93] measured surface stress anisotropy of $80 \pm 30 \text{ meV}/\text{\AA}^2$ at 500 K . Xu et al. [97] applied the theoretical formalism in Ref. [72] to investigate the effect of partial monolayers of Cl on Si(001) surface stress anisotropy and step energies. Anisotropic island shapes have also been observed on the reconstructed GaAs(001) 2×4 surface and on Ising model surfaces [98–100]. For Si(111) at temperatures corresponding to the coexistence of “ 1×1 ” and 7×7 reconstructed phases, elastic force monopoles at the interfaces of the phase domains lead to size-dependent domain shapes [29,33,101–103].

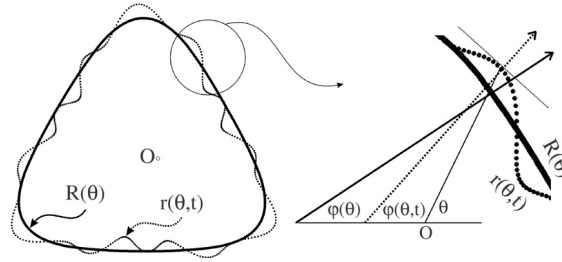


Fig. 8. Schematic diagram illustrating the equilibrium $R(\theta)$ and temporal $r(\theta, t)$ shapes of an anisotropic hexagonal-shaped island. Ref. [58].

2.2. Anisotropic 2D island shape fluctuation analyses

As shown in the previous section, orientation-dependent β values can be determined analytically to within the scale factor λ , the equilibrium chemical potential of the island per unit area, from $R(\theta)$. λ is independent of step orientation and sets the energy scale for mass transport on the surface. The theory of anisotropic shape fluctuations [58] provides a method for determining λ and, hence, absolute $\beta(\varphi)$ values from measurements of temporal fluctuations about 2D equilibrium shapes of both isotropic and highly anisotropic islands. This method has been applied to extract absolute orientation-dependent step energies on TiN(111) [69,70] and Pb(111) [104].

Thermal fluctuations about the equilibrium island shape are caused by random motion of edge atoms and/or adatom attachment/detachment at step edges. As a result, the total step free energy of the island increases. Akutsu and Akutsu [105] have shown that step stiffness $\tilde{\beta}$ is inversely related to the fluctuation width of an island step. Khare and Einstein [59,106] derived a formalism relating shape fluctuations to the step energy for isotropic (i.e., circular) islands. This approach, which is restricted to the case of isotropic, or near-isotropic, island shapes, was applied to determine orientation-averaged step energies on Cu(111), Ag(111), and Cu(001) [50] surfaces. However, even simple elemental metal surfaces are anisotropic. Since the variation of β with φ determines the equilibrium shape of 2D islands and the related property $\tilde{\beta}(\varphi)$ controls 2D island coarsening/decay, coalescence, and shape fluctuation kinetics, knowledge of $\beta(\varphi)$ and $\tilde{\beta}(\varphi)$ is essential.

The symbols R and r in the following discussion refer to the equilibrium island shape $R(\theta)$ and the time-dependent fluctuating shape $r(\theta, t)$. Fig. 8 is a schematic diagram illustrating the relationship between R and r for an anisotropic hexagonal-shaped island. The total free energy $F(t)$ of an island is related to the island shape r through the relationship

$$F(t) = \int_0^{2\pi} d\theta (\beta[\varphi(\theta, t)] \partial_{\theta} s). \quad (8)$$

In Eq. (8), $\partial_{\theta} s = [r^2 + (\partial_{\theta} r)^2]^{1/2}$ is the differential step length element along the island boundary and $\varphi(\theta, t)$ is the angle between the local normal to the fluctuating shape at $r(\theta, t)$ and the x axis, as shown in Fig. 8. $\beta(\varphi)$ in Eq. (8) is also a function of θ and t . Since the equilibrium shape corresponds to the minimum free energy F_0 , temporal deviations $g(\theta, t)$ from the equilibrium shape result in a change in free energy $\Delta F(t) \equiv F(t) - F_0$, where $g \equiv g(\theta, t)$ is defined as in Ref. [50] to be the normalized

deviation of the temporal shape $r \equiv r(\theta, t)$ from the equilibrium shape $R \equiv R(\theta)$. Thus,

$$g \equiv [r - R]/R. \quad (9)$$

In order to derive an expression for λ in terms of the measurable quantity g , a function $f \equiv f(\theta, r, \partial_\theta r)$ is constructed to yield

$$f(\theta, r, \partial_\theta r) = \beta[\varphi(\theta, t)]\partial_\theta s - \lambda(r^2/2) \quad (10)$$

such that $F(t) = \int_0^{2\pi} d\theta[f(\theta, r, \partial_\theta r)]$. The second term in Eq. (10) accounts for the constant area constraint with the Lagrange multiplier λ . Expanding f to second order in r and $\partial_\theta r$ by Taylor's theorem and neglecting higher order terms results in

$$f(\theta, r, \partial_\theta r) = f^0(\theta, R, \partial_\theta R) + f^1(\theta, R, \partial_\theta R) + f^2(\theta, R, \partial_\theta R), \quad (11)$$

where the superscripts to the function f denote the order of differentiation.

For the equilibrium island shape, β and φ are given by Eqs. (2) and (3) with $r \equiv R$, and $\partial_\theta r \equiv \partial_\theta R$. Thus, from Eq. (10), $f^0(\theta, R, \partial_\theta R) = (\lambda R^2)/2$. Note that $f^1(\theta, R, \partial_\theta R) = 0$ is the stability condition for equilibrium. Upon simplification, with β and $\tilde{\beta}$ expressed in terms of R and λ according to Eqs. (2), (3), (4), and (5), Eq. (11) reduces to

$$f(\theta, r, \partial_\theta r) = \frac{\lambda R^2}{2} \left\{ 1 + \frac{R^2 \partial_\theta g^2}{(R^2 + 2(\partial_\theta R)^2 - R \partial_{\theta\theta} R)} - g^2 \right\}. \quad (12)$$

Thus, the fluctuating component of the free energy functional $\Delta F(t)$ is given by

$$\Delta F(t) = -\lambda \int_0^{2\pi} d\theta (P(\theta)g^2 - X(\theta)(\partial_\theta g)^2), \quad (13)$$

with functions $P(\theta)$ and $X(\theta)$ defined as

$$P(\theta) \equiv \frac{R^2}{2} \quad (14)$$

and

$$X(\theta) \equiv \frac{R^4}{2[R^2 + 2(\partial_\theta R)^2 - R \partial_{\theta\theta} R]}. \quad (15)$$

Representing the functions g , $P(\theta)$, and $X(\theta)$ as Fourier series $g = \sum_n g_n(t)e^{in\theta}$, $P(\theta) = \sum_n P_n e^{in\theta}$, and $X(\theta) = \sum_n X_n e^{in\theta}$, respectively, Eq. (13) can be written in terms of the Fourier components $g_n(t)$, X_n , and P_n as

$$\Delta F(t) = -2\pi\lambda \sum_{m,n} [P_{-n-m} + (mn)X_{-n-m}]g_m(t)g_n(t). \quad (16)$$

Note that P_n and X_n in Eq. (16) are independent of time; temporal changes in the total free energy are only due to $g_n(t)$. From the definition of g in Eq. (9), $\langle g(\theta, t) \rangle \equiv g_0(t) \equiv 0$. Thus, for fluctuation modes $m = n = 0$, the summations in Eq. (16) are equal to zero. Furthermore, the equalities $g_n^*(t) \equiv g_{-n}(t)$, $P_n^* \equiv P_{-n}$, and $X_n^* \equiv X_{-n}$, where the superscript $*$ denotes the complex conjugate, guarantee that

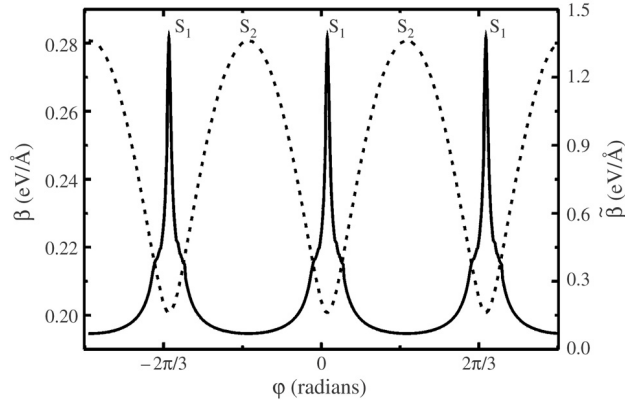


Fig. 9. Absolute values of β versus φ (dashed line) and $\tilde{\beta}$ versus φ (solid line) for a TiN(111) vacancy island at $T_a = 1248$ K. Ref. [70].

the functions g , P , and X are all real and have no imaginary components. Szalma and Einstein [104] expressed $\Delta F(t)$ as a diagonalizable matrix of the form

$$\Delta F[\{g_n\}; t] = 2\pi\lambda \sum_n \Lambda_n g_n g_n^*, \quad (17)$$

where Λ_n in Ref. [104] are the eigenvalues of the matrix $[P_{-n-m} + (mn)X_{-m-n}]$ in Eq. (16) and $\{g_n\}$ denotes $g_n(t)$ at all allowed values of n .

Ignoring the entropic contribution to the free energy yields $\Delta F \approx \Delta U$, where ΔU is the internal energy of the fluctuating island. ΔF has the same functional form as the Hamiltonian $H(\{x_n\})$, a homogeneous function of $\{x_n\}$ which satisfies the condition given by the generalized equipartition theorem [107],

$$\left\langle x_n \frac{\partial H}{\partial x_m} \right\rangle = \delta_{m,n} k_B T, \quad (18)$$

where x_n represents either canonical momenta p_n or coordinates q_n and $\delta_{m,n}$ is the Kronecker delta function. Combining Eqs. (17) and (18) yields an expression for λ in terms of the experimentally measurable parameters R and g as [104]:

$$\lambda = \left(\frac{k_B T}{2} \right) \frac{1}{2\pi \Lambda_n \langle |g_n|^2 \rangle}. \quad (19)$$

Eq. (19), together with Eqs. (2)–(5), can be used to determine absolute values of $\beta(\varphi)$ and $\tilde{\beta}(\varphi)$. The dashed and solid lines in Fig. 9 are typical plots of $\beta(\varphi)$ and $\tilde{\beta}(\varphi)$, in this case for a 2D TiN(111) vacancy island at $T = 1248$ K. For the two $\langle 110 \rangle$ steps, we obtain: $\beta_1 = 0.23 \pm 0.05$ eV/Å and $\tilde{\beta}_1 = 1.9 \pm 1.1$ eV/Å with $\beta_2 = 0.33 \pm 0.07$ eV/Å and $\tilde{\beta}_2 = 0.08 \pm 0.02$ eV/Å over the observed temperature range (1165–1248 K) [69].

An alternate approach to determine absolute step energies, described below, is via the combined analyses of 2D island decay and equilibrium shape measurements.

3. Analyses of 2D island decay (Ostwald ripening) kinetics

The phenomenon of 2D island coarsening/decay or Ostwald ripening [54,108–111], where large 2D clusters grow at the expense of smaller clusters, is described by the Gibbs–Thomson (GT) equation, which relates the equilibrium free adatom concentration ρ^{eq} associated with an island to the equilibrium island chemical potential per unit area λ through the expression

$$\rho^{\text{eq}} = \rho_{\infty}^{\text{eq}} \exp\left(\frac{\lambda \Omega}{kT}\right). \quad (20)$$

$\rho_{\infty}^{\text{eq}}$ is the equilibrium free adatom concentration of a straight step and λ is related to the orientation-dependent island curvature $\kappa(\theta)$ and the step edge stiffness $\tilde{\beta}(\varphi)$ as [54]

$$\lambda = \tilde{\beta}(\varphi)\kappa(\theta), \quad (21)$$

where Ω is the unit atomic area. Smaller islands have higher curvatures, and hence higher adatom concentrations, than larger islands resulting in adatom transfer from small to large islands. Thus, coarsening is simply curvature-driven mass transport. The process involves desorption of the diffusing species from a parent island, migration across the terrace, and attachment at neighboring step edges.

The general phenomenon of Ostwald ripening was first observed using STM on Au surfaces by Jaklevic and Elie [112], Gimzewski, Berndt, and Schlittler [113], and Peale and Cooper [114]. Quantitative investigations of 2D island coarsening/decay kinetics were carried out for Si(001) by Theis et al. [115] using LEEM. Since then, several groups have studied 2D island coarsening/decay kinetics on metal [47,48,75,79,116–130], semiconducting [101,131–137], ceramic [138,139], and metallic compound [49,140–144] surfaces, and at solid–liquid interfaces [145–148]. Unusual coarsening behavior was observed on Au (110) [76,77].

Classical mean-field theory formulations [83,109–111] describing Ostwald ripening kinetics predict power law behavior for island radii as a function of time with exponents of 1/3 for diffusion-limited and 1/2 for detachment-limited kinetics. These simple scaling relations are derived on the basis of the assumptions that the islands are small, the effect of the local adatom environment surrounding the islands is negligible, and that step energies are isotropic.

Accurate determination of adatom transport parameters and step energies from island coarsening/decay kinetics requires either solving the decay rate equations numerically [47,48] or detailed modeling of diffusion-limited decay rates for the entire island ensemble while accounting for differences in local adatom concentrations across the entire surface slab [119,117,149]. However, these procedures are tedious and, quite often, surface boundary conditions are not well-defined in experimental results due to the limited fields of view and the presence of island diffusion and coalescence events. This difficulty can be overcome by employing an elegant and simple approach [120,142] in which a series of isolated island configurations, a single adatom island in a vacancy pit and/or on a larger terrace island are prepared by deposition or sputter-etching.

Two sets of three typical STM images of the decay of a 2D TiN(001) adatom island (light grey) within a single-atom-deep vacancy island (dark grey) and on an isolated single-atom-height terrace are shown in Figs. 10 and 11, respectively [142]. In the diffusion-limited regime, the total energy E_a required to remove an adatom from a step edge is equal to the sum of the adatom formation energy E_f and the activation energy E_s for diffusion on the terrace, as shown schematically in Fig. 12. Island decay in both the above simple isolated island configurations (single adatom islands concentrically placed in a vacancy

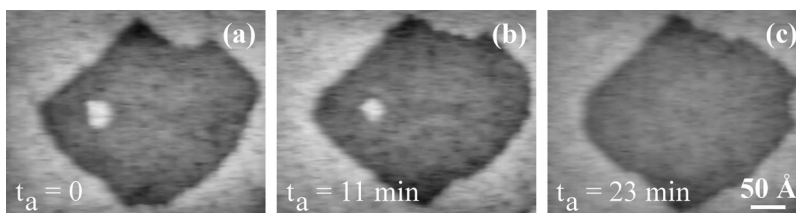


Fig. 10. Scanning tunneling microscopy (STM) images ($375 \times 300 \text{ \AA}^2$) of a single TiN adatom island (light grey) in a vacancy pit (dark grey) at times (a) $t_a = 0$, (b) 11, and (c) 23 min during annealing at $T_a = 1113 \text{ K}$. Ref. [142].

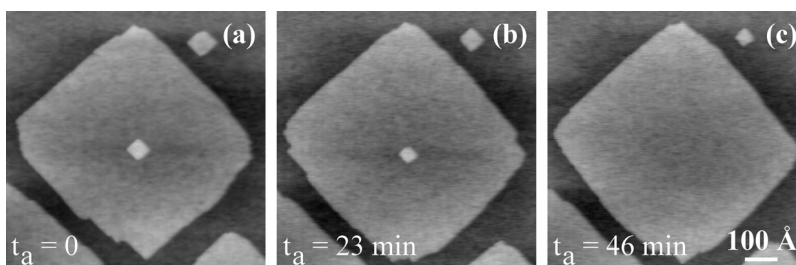


Fig. 11. Three STM images ($800 \times 800 \text{ \AA}^2$) of a single TiN adatom island (light grey) on a terrace (darker grey) at times (a) $t_a = 0$, (b) 23, and (c) 46 min during annealing at $T_a = 1123 \text{ K}$. Ref. [142].

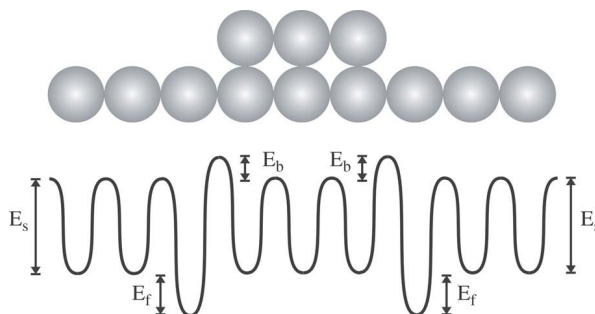


Fig. 12. Schematic diagram of surface activation barriers near an island step edge: E_s is the diffusion barrier, E_f is the adatom formation energy, and E_b is the Ehrlich step edge barrier. Ref. [142].

pit and on a terrace) involves the detachment of adatoms which diffuse across the surrounding terrace to reattach at step edges. However, for the island in the pit, attachment occurs at ascending step edges while, for the terrace island, adatoms have to overcome an additional Ehrlich barrier E_b for adatom transport over step edges leading to attachment at descending steps. The difference in the activation energies for island decay on terraces and in the vacancy pits corresponds to E_b . Since boundary conditions for the island configurations in Figs. 10 and 11 are given exactly by the Gibbs–Thomson relation in Eq. (20), adatom transport parameters, the Ehrlich barrier, and step energies can be determined accurately from time- and temperature-dependent measurements of island decay.

However, for anisotropic islands, where $\tilde{\beta}$ is a strong function of φ , the modeling of island dissolution kinetics using Eqs. (20) and (21) requires the calculation of orientation-dependent island curvature at

each time step and a priori knowledge of $\tilde{\beta}(\varphi)$. This approach is computationally intensive, prone to errors, as the calculations are carried out on a discrete set of island shape data, and cannot be employed if $\tilde{\beta}(\varphi)$ is unknown.

3.1. Modified Gibbs–Thomson relation for anisotropic islands

Here, a modified expression for the Gibbs–Thomson relation is derived that simplifies the analysis for anisotropic island decay kinetics. $\kappa(\theta)$ in Eq. (21) can be expressed by the relation

$$\kappa(\theta) = \frac{S(\theta)}{r_{\text{avg}}}, \quad (22)$$

where

$$S(\theta) = \frac{\{[r(\theta)/r_{\text{avg}}]^2 + 2[\partial_\theta r/r_{\text{avg}}]^2 - [r(\theta)\partial_{\theta\theta} r/r_{\text{avg}}^2]\}}{\{[r(\theta)/r_{\text{avg}}]^2 + [\partial_\theta r/r_{\text{avg}}]^2\}^{3/2}} \quad (23)$$

is a dimensionless orientation-dependent curvature function describing the equilibrium shape and $r_{\text{avg}} = \sqrt{A/\pi}$ is the average island radius. Combining Eqs. (4) and (21)–(23), an exact expression for λ is obtained in terms of the *orientation-independent* parameters r_{avg} and B [71]:

$$\lambda = \frac{B}{r_{\text{avg}}}, \quad (24)$$

with

$$B \equiv \tilde{\beta}(\varphi)S(\theta). \quad (25)$$

B , defined in Eq. (25), determines the energy scale of the surface equilibrium chemical potential.

It is important to note that the parameter B is related to, but not equal to, the orientation-averaged step energy β_{avg} , defined as $\beta_{\text{avg}} = \frac{1}{2\pi} \int_0^{2\pi} \beta(\varphi) d\varphi$. Using the transformation $\partial_\theta \varphi = \kappa(\theta) \sqrt{(R^2 + \partial_\theta^2 R)}$ derived from Eq. (3), together with Eqs. (2) and (24), we find that $\beta_{\text{avg}} = \frac{B}{2\pi r_{\text{avg}}^2} \int_0^{2\pi} R^2(\theta) S(\theta) d\theta$. Eq. (20) can now be written in terms of B and r_{avg} as [71]

$$\rho^{\text{eq}} = \rho_\infty^{\text{eq}} \exp\left(\frac{B\Omega}{r_{\text{avg}}kT}\right). \quad (26)$$

For the case of isotropic (circular) islands, $B = \beta$ and $r_{\text{avg}} = \tilde{r}$ and the isotropic GT equation, $\rho^{\text{eq}} = \rho_\infty^{\text{eq}} \exp(\beta\Omega/\tilde{r}kT)$, is recovered. Note that Eq. (26), while analogous to the GT relation for a circular island, is an *exact* expression that is valid for anisotropic islands with *any* arbitrary equilibrium island shape. More importantly, Eq. (26) provides a convenient and simple approach for modeling the coarsening/decay kinetics of *anisotropic* islands based on the measurable parameters B and r_{avg} .

Fig. 13(a) and (b) are plots of r_{avg} versus annealing time t_a for the 2D TiN(001) adatom island in a vacancy pit shown in Fig. 10 and the TiN(001) adatom island on a terrace in Fig. 11, respectively. The open circles are the measured data, while the solid lines are calculated curves using the least squares best fit value for B , 0.23 eV, obtained using the diffusion-limited island decay model described in Ref. [142] to fit STM data for TiN(001) island decay. These results, together with the relative $\beta(\varphi)$

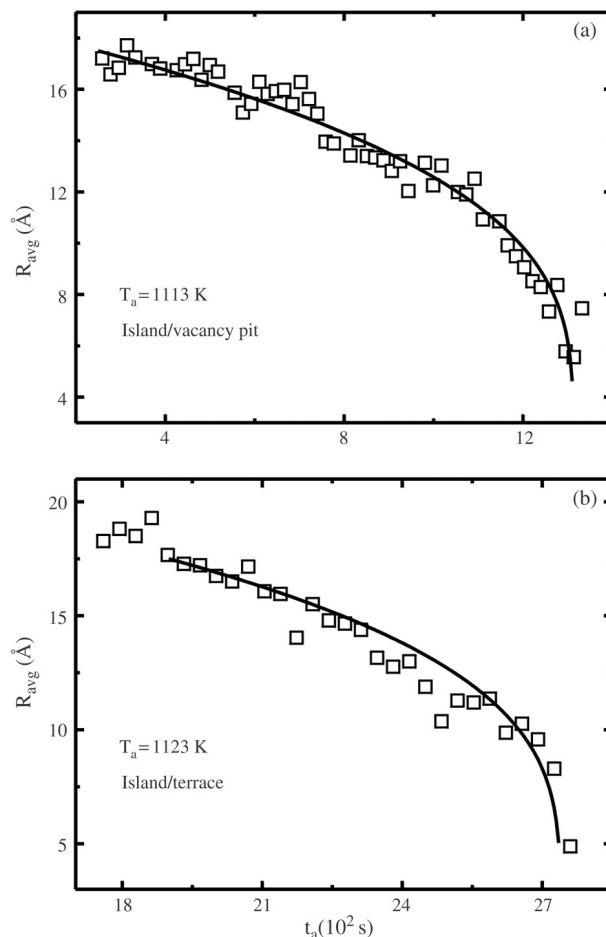


Fig. 13. r_{avg} versus t_a plots for (a) the adatom island in a vacancy pit shown in Fig. 10 and (b) the adatom island on a terrace shown in Fig. 11. The open squares are measured data, while the solid lines are obtained using the diffusion-limited island decay model with $B = 0.23$ eV/Å. Ref. [142].

data for TiN(001) islands in Fig. 4(b) obtained from the 2D equilibrium island shape analyses described in Section 2, are used to extract absolute orientation-dependent step energies and step stiffnesses. For $\langle 110 \rangle$ and $\langle 100 \rangle$ steps on TiN(001), we obtain: $\beta_{110} = 0.21 \pm 0.05$ eV/Å, $\beta_{100} = 0.25 \pm 0.05$ eV/Å, $\tilde{\beta}_{110} = 0.9 \pm 0.2$ eV/Å, and $\tilde{\beta}_{100} = 0.07 \pm 0.02$ eV/Å [71]. Complete $\beta(\varphi)$ and $\tilde{\beta}(\varphi)$ data for TiN(001) are shown in Fig. 14.

Information concerning the variation of $\tilde{\beta}$ with φ is essential for the analysis of island coalescence whose kinetics are also controlled by step stiffness, as discussed below.

4. Anisotropic 2D island coalescence kinetics

Island coalescence, driven by step edge energy minimization, occurs during film growth or annealing when two or more islands contact each other as a consequence of coarsening and/or island diffusion.

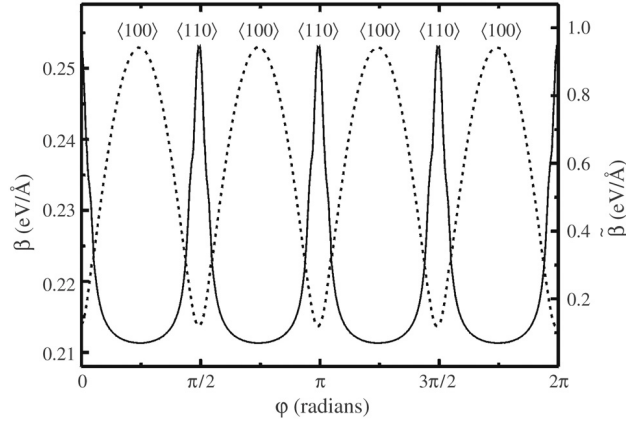


Fig. 14. Absolute values of β versus φ (dashed line) and $\tilde{\beta}$ versus φ (solid line) for a TiN(001) vacancy island at $T_a = 1140$ K. Ref. [71].

Subsequent reshaping of the coalesced island toward its equilibrium shape requires mass transport whose kinetics depend on one or more of the following mechanisms: edge diffusion, attachment/detachment at island step edges, and surface diffusion. The equilibration kinetics of 1D step [150–152] and 2D island [151,153] shapes formed due to step–island and island–island coalescence, respectively, on (100) and (111) fcc surfaces have been studied experimentally using STM. Kinetic Monte Carlo simulations [151,154,155] and continuum models [156,157], based on Mullin’s theory for surface relaxation [54], have also been used to investigate the relaxation kinetics of far-from-equilibrium structures. In this section, we review recent progress in quantitative analyses of 2D anisotropic island reshaping kinetics and extraction of edge-atom mass transport parameters.

In a continuum model for 2D island shape evolution via edge diffusion [155], the normal component v_n of the step edge velocity is related to the step chemical potential μ as

$$v_n(\varphi, t) = \left(\frac{\Omega \sigma_{\text{edge}}}{kT} \right) \nabla_s^2 \mu(\varphi, t). \quad (27)$$

φ in Eq. (27) is the local step orientation, i.e. the angle of the local step normal, $\nabla_s = [(\partial_s x)^2 + (\partial_s y)^2]^{-1/2} \partial_s$, in which s is the arc length element along the island boundary $[x(s, t), y(s, t)]$ and σ_{edge} is the edge mobility of the diffusing species. Expressing μ in terms of the step curvature $\kappa(s, t)$ and step stiffness $\tilde{\beta}(\varphi)$ as $\mu(\varphi, t) = \tilde{\beta}(\varphi) \kappa(s, t) \Omega$ yields

$$v_n(\varphi, t) = C \nabla_s^2 [\kappa(s, t) \tilde{\beta}(\varphi)] \quad (28)$$

with $C = \sigma_{\text{edge}} \Omega^2 / kT$. For an isotropic (circular) island, where $\tilde{\beta}(\varphi) \equiv \beta$ is a constant, Eq. (28) reduces to a mathematical representation of the Laplacian of curvature-driven 2D surface evolution [158]. For anisotropic islands, however, $\tilde{\beta}(\varphi)$ varies with step orientation and Eq. (28) must be used in its exact form. If σ_{edge} is also a function of φ , then the solution of Eq. (28) depends on the functional form of σ_{edge} . For convenience, σ_{edge} is assumed to be independent of step orientation in the numerical procedure described below.

Imaging techniques such as STM and LEEM are commonly used to obtain non-equilibrium island shapes as a function of annealing time t_a and temperature T_a . Fig. 15(a)–(d) consists of two sets of four

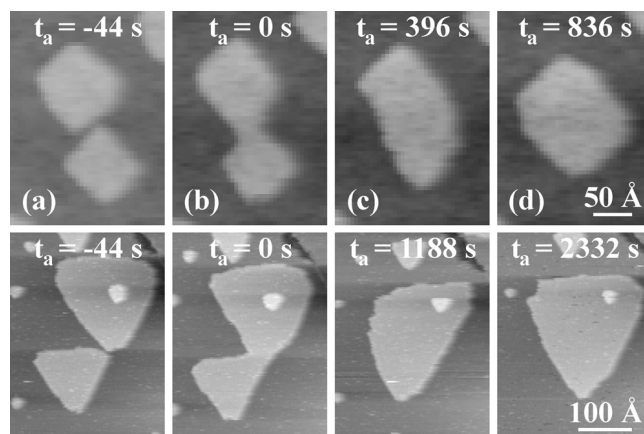


Fig. 15. (a)–(d): Representative STM images, acquired at 44 s/frame, showing coalescence and subsequent reshaping of 2D TiN adatom islands during annealing: (upper panel) TiN(001), $T_a = 1123$ K, scan size = $220 \times 320 \text{ \AA}^2$; (lower panel) TiN(111), $T_a = 1146$ K, scan size = $290 \times 330 \text{ \AA}^2$. Ref. [159].

representative STM images showing 2D TiN adatom island coalescence and subsequent shape evolution on atomically smooth (001) (upper panels) and (111) (lower panels) TiN terraces as a function of annealing time t_a [159]. Both sets of images were acquired at a rate of 44 s/frame. We define $t_a = 0$ as the time at which the first image (Fig. 15(b)) of the coalesced island was acquired. The two square TiN(001) islands shown in the upper panel of Fig. 15(a) initiate coalescence at corner $\langle 100 \rangle$ steps and form a “figure-eight” shaped island (Fig. 15(b)), with area $A = 1.1 \times 10^4 \text{ \AA}^2$ and perimeter $L(t_a = 0 \text{ s}) = 480 \text{ \AA}$, which relaxes to its equilibrium shape in ≈ 840 s (Fig. 15(d)). Truncated-hexagonal TiN(111) islands shown in the lower panel of Fig. 15(a) coalesce at corner $\langle 110 \rangle$ steps resulting in a “saw-tooth” shape (figure Fig. 15(b)) with $A = 3.6 \times 10^4 \text{ \AA}^2$ and $L(t_a = 0 \text{ s}) = 934 \text{ \AA}$. The coalesced (111) island reaches its equilibrium shape in ≈ 2330 s (see Fig. 15(d)). Experimentally determined values for the island perimeter L are plotted in Fig. 16(a) and (b) as a function of t_a during the relaxation of the coalesced TiN(001) and TiN(111) adatom islands shown in Fig. 15. In both cases, L decreases monotonically to a minimum value L_{eq} corresponding to the equilibrium island shape.

From the images, island boundaries are determined. The boundary coordinates of the $t_a = 0$ image are represented by a series of equally spaced points $[x(s), y(s)]$ separated by s . At each time step Δt , a finite difference approximation is used to compute the first and second spatial derivatives $[x_s, y_s]$ and $[x_{ss}, y_{ss}]$ at positions $[x(s), y(s)]$ along the boundary. The step orientation $\varphi(t_a)$ and curvature $\kappa(s, t_a)$ are then determined from the expressions $\varphi(s, t_a) = \arctan(-x_s/y_s)$ and $\kappa = (x_s y_{ss} - x_{ss} y_s)/(x_s^2 + y_s^2)^{3/2}$, respectively. $\tilde{\beta}[\varphi(s, t_a)]$ values for all step orientations $\varphi(s, t_a)$ are interpolated from $\tilde{\beta}(\varphi)$ data. The step edge velocities $v_n = [\Delta x/\Delta t, \Delta y/\Delta t] \cdot \hat{\mathbf{n}}(s, t_a)$, where $\hat{\mathbf{n}}(s, t_a)$ is the unit normal vector to the arc s at t_a , are then obtained. New boundary coordinates $[x + \Delta x, y + \Delta y]$ and the island perimeter L are calculated as a function of time until L reaches a minimum value corresponding to the equilibrium island shape.

In solving Eq. (28), the only free parameter is the quantity $\tau = C\Delta t$, where C and Δt are inversely related to each other. The parameter C , and hence the edge mobility σ_{edge} , is determined by comparing the calculated shapes $S_{\text{calc}}(\tau) \equiv [x(s, \tau), y(s, \tau)]$ with the experimentally measured island shapes $S_{\text{exp}}(t_a) \equiv [x(s, t_a), y(s, t_a)]$ using the following procedure. A characteristic function $f_n(x, y)$ ($n = 1$

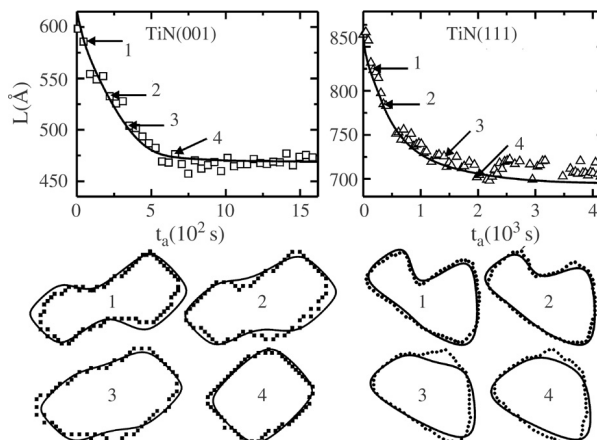


Fig. 16. Upper panel: island perimeter L plotted as a function of annealing time t_a for the (a) TiN(001) and (b) TiN(111) adatom islands shown in Fig. 15. Lower panel: time-dependent shapes of the islands labeled 1, 2, 3, and 4 in the upper panel. Symbols are experimental data while solid lines are calculated curves obtained using (Eq. (28)). Ref. [159].

or 2) is defined such that, for a given set of points (x, y) , $f_n(x, y) = (-1)^{n-1}$ if (x, y) is inside the curves S_{exp} and S_{calc} and $f_n(x, y) = 0$ if (x, y) is outside the curves S_{exp} and S_{calc} . A new function $h(x, y) = |f_1(x, y) + f_2(x, y)|$ is then defined such that $h(x, y) = 1$ for the set of points (x, y) that are simultaneously inside (outside) S_{calc} and outside (inside) S_{exp} and $h(x, y) = 0$ if (x, y) is either inside or outside both S_{calc} and S_{exp} . A measure of the agreement between the two curves S_{calc} and S_{exp} is then given by $H = \iint dx dy h(x, y)$, where $H = 0$ corresponds to $S_{\text{calc}} \equiv S_{\text{exp}}$. H values are determined by comparing calculated island shapes $S_{\text{calc}}(\tau)$ at all steps τ with the experimental data $S_{\text{exp}}(t_a)$ at each t_a . The minimum value $H_{\text{min}}(t_a, \tau_{\text{calc}})$ yields the calculated parameter τ_{calc} for which best fits are obtained between $S_{\text{calc}}(\tau_{\text{calc}})$ and the experimental data $S_{\text{exp}}(t_a)$. Calculated island perimeters L , plotted as solid lines in Fig. 16(a) and (b) as a function of τ_{calc}/C for TiN(001) and TiN(111) islands, are in good agreement with the experimental data. The lower panels in Fig. 16 show typical calculated curves (solid lines) and experimentally determined island shapes (dotted lines) at the times labeled 1–4 in the upper panels. From the τ_{calc} values, we obtain orientation-averaged edge-atom mobilities σ_{edge} of $21.7 \pm 0.4 \text{ \AA/s}$ for TiN(001) and $36 \pm 1.1 \text{ \AA/s}$ for TiN (111) [159]. For comparison, the adatom mobilities are $\approx 4.9 \times 10^{-2} \text{ \AA/s}$ and $7.8 \times 10^{-2} \text{ \AA/s}$ for diffusion- and detachment-limited decay of 2D TiN adatom islands on (001) and (111) TiN terraces, respectively [141,142]. These results indicate that edge-atom mobilities on (001) and (111) TiN terraces are faster than terrace adatom mobilities.

5. Conclusions

In this report, we reviewed recent progress toward developing generalized theoretical and experimental approaches elucidating the effects of step edge energy anisotropy on the temperature-dependent dynamics of 2D anisotropic islands. Specifically, we focussed on the kinetics of 2D island coarsening/decay (Ostwald ripening), temporal fluctuations about equilibrium island shapes, and shape relaxation following island coalescence in anisotropic systems. We presented a combination of experimental and theoretical methods for the determination of absolute orientation dependent step

energies and step stiffnesses, which are required for the quantitative description of highly anisotropic island dynamics.

This report is intended to complement and extend the existing literature on isotropic island dynamics and to be useful for analyzing surface dynamics on anisotropic (i.e., “real”) material surfaces. With the recent surge of interest in the synthesis and characterization of nanostructures, there is a growing need for an understanding of the atomic-scale mechanisms governing nanostructure stability. Hence, the existing formalism describing anisotropic 2D island dynamics should be extended to the analysis of anisotropic 3D nanostructures.

Acknowledgements

The authors gratefully acknowledge the financial support of the US Department of Energy under Contract No. DEFG02-91ER45439. We also appreciate the use of the facilities in the Center for Microanalysis of Materials, partially supported by DOE, at the University of Illinois.

References

- [1] G. Binnig, H. Rohrer, C. Gerber, *Appl. Phys. Lett.* 40 (1982) 178.
- [2] G. Binnig, C.F. Quate, C. Gerber, *Phys. Rev. Lett.* 56 (1986) 930.
- [3] E.W. Müller, *Z. Phys.* 131 (1951) 136.
- [4] S.C. Wang, G. Ehrlich, *Phys. Rev. Lett.* 79 (1997) 4234.
- [5] S.C. Wang, U. Kürpick, G. Ehrlich, *Phys. Rev. Lett.* 81 (1998) 4923.
- [6] G. Ehrlich, *Surf. Sci.* 331–333 (1995) 865 (and references therein).
- [7] F. Besenbacher, P.T. Sprunger, L. Ruan, L. Olesen, I. Stensgaard, E. Lægsgaard, *Top. Catal.* 1 (1994) 325.
- [8] L. Petersen, M. Schunack, B. Schaefer, T.R. Linderoth, P.B. Rasmussen, P.T. Sprunger, E. Lægsgaard, I. Stensgaard, F. Besenbacher, *Rev. Sci. Instrum.* 72 (2001) 1438.
- [9] E. Lægsgaard, L. Österlund, P. Thstrup, P.B. Rasmussen, I. Stensgaard, F. Besenbacher, *Rev. Sci. Instrum.* 72 (2001) 3537.
- [10] K. Morgenstern, *Phys. Status Solidi (b)* 242 (2005) 773.
- [11] M.J. Rost et al., *Rev. Sci. Instrum.* 76 (2005) 053710.
- [12] J. de la Figuera, J.E. Prieto, C. Ocal, R. Miranda, *Solid State Commun.* 89 (1994) 815.
- [13] J.-M. Wen, S.-L. Chang, J.W. Burnett, J.W. Evans, P.A. Thiel, *Phys. Rev. Lett.* 73 (1994) 2591.
- [14] K. Morgenstern, G. Rosenfeld, B. Poelsema, G. Comsa, *Phys. Rev. Lett.* 74 (1995) 2058.
- [15] J.-M. Wen, J.W. Evans, M.C. Bartelt, J.W. Burnett, P.A. Thiel, *Phys. Rev. Lett.* 76 (1996) 652.
- [16] C.R. Stoldt, C.J. Jenks, P.A. Thiel, A.M. Cadilhe, J.W. Evans, *J. Chem. Phys.* 111 (1999) 5157.
- [17] W.W. Pai, A.K. Swan, Z. Zhang, J.F. Wendelken, *Phys. Rev. Lett.* 79 (1997) 3210.
- [18] T.R. Linderoth, S. Horch, L. Petersen, S. Helveg, E. Lægsgaard, I. Stensgaard, F. Besenbacher, *Phys. Rev. Lett.* 82 (1999) 1494.
- [19] K. Morgenstern, E. Lægsgaard, F. Besenbacher, *Phys. Rev. Lett.* 86 (2001) 5739.
- [20] K. Morgenstern, E. Lægsgaard, F. Besenbacher, *Phys. Rev. B* 66 (2002) 115408.
- [21] D. Schlößer, K. Morgenstern, L.K. Verheij, G. Rosenfeld, F. Besenbacher, G. Comsa, *Surf. Sci.* 465 (2000) 19.
- [22] Y.W. Mo, J. Kleiner, M.B. Webb, M.G. Lagally, *Phys. Rev. Lett.* 66 (1991) 1998.
- [23] H. Brune, H. Röder, C. Boragno, K. Kern, *Phys. Rev. Lett.* 73 (1994) 1955.
- [24] H. Brune, H. Röder, K. Bromann, K. Kern, *Thin Solid Films* 264 (1995) 230.
- [25] H.H. Teng, P.M. Dove, C.A. Orme, J.J. De Yoreo, *Science* 282 (1998) 724.
- [26] C.M. Pina, U. Becker, P. Risthaus, D. Bosbach, A. Putnis, *Nature* 395 (1998) 483.
- [27] E. Bauer, *Rep. Prog. Phys.* 57 (1994) 895.
- [28] A.K. Schmidt, N.C. Bartelt, R.Q. Hwang, *Science* 290 (2000) 1561.

- [29] J.B. Hannon, R.M. Tromp, *Annu. Rev. Mater. Res.* 33 (2003) 263.
- [30] G. Ertl, H.H. Rotermund, *Curr. Opin. Solid State Mater. Sci.* 1 (1996) 617.
- [31] M. Zinke-Allmang, L.C. Feldman, M.H. Grabow, *Surf. Sci. Rep.* 16 (1992) 377.
- [32] M. Zinke-Allmang, *Thin Solid Films* 346 (1999) 1.
- [33] R.M. Tromp, J.B. Hannon, *Surf. Rev. Lett.* 9 (2002) 1565.
- [34] H.-C. Jeong, E.D. Williams, *Surf. Sci. Rep.* 34 (1999) 171.
- [35] M. Giesen, *Prog. Surf. Sci.* 68 (2001) 1 (and references therein).
- [36] M. Nowicki, A. Emundts, H.P. Bonzel, *Prog. Surf. Sci.* 74 (2003) 123.
- [37] H.P. Bonzel, *Phys. Rep.* 385 (2003) 1.
- [38] H.P. Bonzel, *Prof. Surf. Sci.* 67 (2001) 45.
- [39] B.S. Swartzentruber, Y.-W. Mo, R. Kariotis, M.G. Lagally, M.B. Webb, *Phys. Rev. Lett.* 65 (1990) 1913.
- [40] N.C. Bartelt, R.M. Tromp, E.D. Williams, *Phys. Rev. Lett.* 73 (1994) 1656.
- [41] D.J. Eaglesham, A.E. White, L.C. Feldman, N. Moriya, D.C. Jacobson, *Phys. Rev. Lett.* 70 (1993) 1643.
- [42] H.P. Bonzel, A. Emundts, *Phys. Rev. Lett.* 84 (2000) 5804.
- [43] K. Arenhold, S. Surnev, H.P. Bonzel, P. Wynblatt, *Surf. Sci.* 424 (1999) 271.
- [44] G.S. Icking-Konert, M. Giesen, H. Ibach, *Phys. Rev. Lett.* 83 (1999) 3880.
- [45] M. Giesen, C. Steimer, H. Ibach, *Surf. Sci.* 471 (2001) 80.
- [46] A. Emundts, M. Nowicki, H.P. Bonzel, *Surf. Sci.* 496 (2002) L35.
- [47] K. Morgenstern, G. Rosenfeld, G. Comsa, *Phys. Rev. Lett.* 76 (1996) 2113.
- [48] G.S. Icking-Konert, M. Giesen, H. Ibach, *Surf. Sci.* 398 (1998) 37.
- [49] S. Kodambaka, V. Petrova, A. Vailionis, P. Desjardins, D.G. Cahill, I. Petrov, J.E. Greene, *Surf. Rev. Lett.* 7 (2000) 589.
- [50] D.C. Schlößer, L.K. Verheij, G. Rosenfeld, G. Comsa, *Phys. Rev. Lett.* 82 (1999) 3843.
- [51] C. Steimer, M. Giesen, L. Verheij, H. Ibach, *Phys. Rev. B* 64 (2001) 085416.
- [52] H.J.W. Zandvliet, *Rev. Modern Phys.* 72 (2000) 593.
- [53] H.J.W. Zandvliet, *Phys. Rep.* 388 (2003) 1.
- [54] W.W. Mullins, *Interface Sci.* 9 (2001) 9.
- [55] H. van Beijeren, I. Nolden, *Topics in Current Physics*, vol. 43, Springer, Berlin, 1987, 259.
- [56] M. Wortis, in: R. Vanselow, R.F. Howe (Eds.), *Chemistry and Physics of Solid Surfaces VII*, Springer, New York, 1988, p. 367.
- [57] P. Nozières, in: C. Godrèche (Ed.), *Solids Far From Equilibrium*, Cambridge University Press, Cambridge, England, 1992, p. 1.
- [58] S.V. Khare, S. Kodambaka, D.D. Johnson, I. Petrov, J.E. Greene, *Surf. Sci.* 522 (2003) 75.
- [59] S.V. Khare, T.L. Einstein, *Phys. Rev. B* 54 (1996) 11752.
- [60] N. Akutsu, Y. Akutsu, *J. Phys. Condens. Matter* 11 (1999) 6635.
- [61] N. Akutsu, Y. Akutsu, *Surf. Sci.* 376 (1997) 92.
- [62] R.K.P. Zia, *J. Stat. Phys.* 45 (1986) 801.
- [63] R.K.P. Zia, J.E. Avron, *Phys. Rev. B* 25 (1982) 2042.
- [64] C. Rottman, M. Wortis, *Phys. Rev. B* 29 (1984) 328.
- [65] C. Rottman, M. Wortis, *Phys. Rep.* 103 (1984) 59.
- [66] T.J. Stasevich, T.L. Einstein, R.K.P. Zia, M. Giesen, H. Ibach, F. Szalma, *Phys. Rev. B* 70 (2004) 245404.
- [67] M. Holzer, *Phys. Rev. Lett.* 64 (1990) 653.
- [68] M. Holzer, *Phys. Rev. B* 42 (1990) 10570.
- [69] S. Kodambaka, V. Petrova, S.V. Khare, D.D. Johnson, I. Petrov, J.E. Greene, *Phys. Rev. Lett.* 88 (2002) 146101.
- [70] S. Kodambaka, S.V. Khare, V. Petrova, D.D. Johnson, I. Petrov, J.E. Greene, *Phys. Rev. B* 67 (2003) 035409.
- [71] S. Kodambaka, V. Petrova, S.V. Khare, A. Vailionis, I. Petrov, J.E. Greene, *Surf. Sci.* 513 (2002) 468.
- [72] A. Li, F. Liu, M.G. Lagally, *Phys. Rev. Lett.* 85 (2000) 1922.
- [73] M.T. Middel, H.J.W. Zandvliet, B. Poelsema, *Phys. Rev. Lett.* 88 (2002) 196105.
- [74] G.J. Xu, S.V. Khare, K.S. Nakayama, C.M. Aldo, J.H. Weaver, *Phys. Rev. B* 68 (2003) 235318.
- [75] M.J. Rost, R. van Gastel, J.W.M. Frenken, *Phys. Rev. Lett.* 84 (2000) 1966.
- [76] M.J. Rost, S.B. van Albada, J.W.M. Frenken, *Phys. Rev. Lett.* 86 (2001) 5938.
- [77] M.J. Rost, S.B. van Albada, J.W.M. Frenken, *Surf. Sci.* 518 (2002) 21.
- [78] S.B. van Albada, M.J. Rost, J.W.M. Frenken, *Phys. Rev. B* 65 (2002) 205421.

- [79] M.J. Rost, S.B. van Albada, J.W.M. Frenken, *Surf. Sci.* 515 (2002) 344.
- [80] N. Akutsu, Y. Akutsu, *J. Phys. Soc. Japan* 64 (1995) 736.
- [81] I. Vilfan, *Surf. Sci.* 350 (1996) 329.
- [82] E. Carlon, H. van Beijeren, *Phys. Rev. Lett.* 76 (1996) 4191.
- [83] J.G. McLean, B. Krishnamachari, D.R. Peale, E. Chason, J.P. Sethna, B.H. Cooper, *Phys. Rev. B* 55 (1997) 1811.
- [84] O.L. Alerhand, D. Vanderbilt, R.D. Meade, J.D. Joannopoulos, *Phys. Rev. Lett.* 61 (1988) 1973.
- [85] O.L. Alerhand, D. Vanderbilt, R.D. Meade, J.D. Joannopoulos, *J. Vac. Sci. Technol. B* 7 (1989) 1013.
- [86] V.I. Marchenko, A.Y. Parshin, *Sov. Phys. JETP* 52 (1980) 129.
- [87] J. Dabrowski, S. Pehlke, M. Scheffler, *J. Vac. Sci. Technol. B* 12 (1994) 2675.
- [88] J. Dabrowski, S. Pehlke, M. Scheffler, *Phys. Rev. B* 49 (1994) 4790.
- [89] A. Garcia, J.E. Northrup, *Phys. Rev. B* 48 (1993) 17350.
- [90] K.O. Ng, D. Vanderbilt, *Phys. Rev. B* 52 (1995) 2177.
- [91] P. Zeppenfeld, M.I. Krzyzowski, C. Romainczyk, G. Comsa, M.G. Lagally, *Phys. Rev. Lett.* 72 (1994) 2737.
- [92] V. Zielasek, F. Liu, Y. Zhao, J.B. Maxson, M.G. Lagally, *Phys. Rev. B* 64 (2001) R201320.
- [93] M.T. Middel, H.J.W. Zandvliet, B. Poelsema, *Phys. Rev. Lett.* 88 (2002) 196105.
- [94] J. Dabrowski, S. Pehlke, M. Scheffler, *J. Vac. Sci. Technol. B* 12 (1994) 2675.
- [95] J. Dabrowski, S. Pehlke, M. Scheffler, *Phys. Rev. B* 49 (1994) 4790.
- [96] A. Garcia, J.E. Northrup, *Phys. Rev. B* 48 (1993) 17350.
- [97] G.J. Xu, S.V. Khare, K.S. Nakayama, C.M. Aldo, J.H. Weaver, *Phys. Rev. B* 68 (2003) 235318.
- [98] V.P. LaBella, D.W. Bullock, M. Anser, Z. Ding, C. Emery, L. Bellaiche, P.M. Thibado, *Phys. Rev. Lett.* 84 (2000) 4152.
- [99] V.P. LaBella, Z. Ding, D.W. Bullock, C. Emery, P.M. Thibado, *J. Vac. Sci. Technol. B* 19 (2001) 1640.
- [100] Z. Ding, D.W. Bullock, P.M. Thibado, V.P. LaBella, K. Mullen, *Phys. Rev. Lett.* 90 (2003) 216109.
- [101] J.B. Hannon, H. Hibino, N.C. Bartelt, B.S. Swartzentruber, T. Ogino, G.L. Kellogg, *Nature* 405 (2000) 552.
- [102] J.B. Hannon, J. Tersoff, R.M. Tromp, *Science* 295 (2002) 299.
- [103] G.E. Thayer, J.B. Hannon, R.M. Tromp, *Nat. Mater.* 3 (2004) 95.
- [104] F. Szalma, H. Gebremariam, T.L. Einstein, *Phys. Rev. B* 71 (2005) 035422.
- [105] Y. Akutsu, N. Akutsu, *J. Phys. A* 19 (1986) 2813.
- [106] S.V. Khare, N.C. Bartelt, T.L. Einstein, *Phys. Rev. Lett.* 75 (1996) 2148.
- [107] K. Huang, *Statistical Mechanics*, Wiley Eastern Limited, 1963, p. 149.
- [108] C. Herring, in: W.E. Kingston (Ed.), *The Physics of Powder Metallurgy*, McGraw-Hill, New York, 1951, p. 143.
- [109] I.M. Lifshitz, V.V. Slyozov, *J. Phys. Chem. Solids* 19 (1961) 35.
- [110] B.K. Chakraverty, *J. Phys. Chem. Solids* 28 (1967) 2401.
- [111] P. Wynblatt, N.A. Gjostein, in: J.O. McCaldin, G. Somorjai (Eds.), *Prog. Solid State Chem.* 9 (1975), 21.
- [112] R.C. Jaklevic, L. Elie, *Phys. Rev. Lett.* 60 (1988) 120.
- [113] J.K. Gimzewski, R. Berndt, R.R. Schlittler, *Phys. Rev. B* 45 (1992) 6844.
- [114] D.R. Peale, B.H. Cooper, *J. Vac. Sci. Technol. A* 10 (1992) 2210.
- [115] W. Theis, N.C. Bartelt, R.M. Tromp, *Phys. Rev. Lett.* 75 (1995) 3328.
- [116] G. Rosenfeld, K. Morgenstern, I. Beckmann, W. Wulfhekel, E. Lægsgaard, F. Besenbacher, G. Comsa, *Surf. Sci.* 402–404 (1998) 401.
- [117] K. Morgenstern, G. Rosenfeld, G. Comsa, *Surf. Sci.* 441 (1999) 289.
- [118] J.B. Hannon, C. Klünker, M. Giesen, H. Ibach, N.C. Bartelt, J.C. Hamilton, *Phys. Rev. Lett.* 79 (1997) 2506.
- [119] N.C. Bartelt, W. Theis, R.M. Tromp, *Phys. Rev. B* 54 (1996) 11741.
- [120] K. Morgenstern, G. Rosenfeld, E. Lægsgaard, F. Besenbacher, G. Comsa, *Phys. Rev. Lett.* 80 (1998) 556.
- [121] C. Klünker, J.B. Hannon, M. Giesen, H. Ibach, G. Boisvert, L.J. Lewis, *Phys. Rev. B* 58 (1998) R7556.
- [122] M. Giesen, H. Ibach, *Surf. Sci.* 431 (1999) 109.
- [123] M. Giesen, *Surf. Sci.* 441 (1999) 391.
- [124] S. Rusponi, C. Boragno, R. Ferrando, F. Hontinfinde, U. Valbusa, *Surf. Sci.* 440 (1999) 451.
- [125] K. Morgenstern, E. Lægsgaard, I. Stensgaard, F. Besenbacher, *Phys. Rev. Lett.* 83 (1999) 1613.
- [126] M. Giesen, G.S. Icking-Konert, H. Ibach, *Phys. Rev. Lett.* 80 (1998) 552.
- [127] M. Giesen, G.S. Icking-Konert, H. Ibach, *Phys. Rev. Lett.* 82 (1999) 3101.
- [128] M. Giesen, H. Ibach, *Surf. Sci.* 464 (2000) L697.

- [129] K. Morgenstern, G. Rosenfeld, G. Comsa, M.R. Sørensen, B. Hammer, E. Lægsgaard, F. Besenbacher, *Phys. Rev. B* 63 (2001) 045412.
- [130] K. Thurmer, J.E. Reutt-Robey, E.D. Williams, M. Uwaha, A. Emundts, H.P. Bonzel, *Phys. Rev. Lett.* 87 (2001) 186102.
- [131] S. Tanaka, N.C. Bartelt, C.C. Umbach, R.M. Tromp, J.M. Blakely, *Phys. Rev. Lett.* 78 (1997) 3342.
- [132] A. Ichimaya, Y. Tanaka, K. Ishimaya, *Phys. Rev. Lett.* 76 (1996) 4721.
- [133] A. Ichimaya, Y. Tanaka, K. Ishimaya, *Surf. Sci.* 386 (1997) 182.
- [134] A. Ichimaya, K. Hayashi, E.D. Williams, T.L. Einstein, M. Uwaha, K. Watanabe, *Phys. Rev. Lett.* 84 (2000) 3662.
- [135] S. Hildebrandt, A. Kraus, R. Kulla, G. Wilhelm, M. Hanbücken, H. Neddermeyer, *Surf. Sci.* 486 (2001) 24.
- [136] H. Hibino, C.-W. Hu, T. Ogino, I.S.T. Tsong, *Phys. Rev. B* 63 (2001) 245402.
- [137] F. Watanabe, S. Kodambaka, W. Swiech, J.E. Greene, D.G. Cahill, *Surf. Sci.* 572 (2004) 425.
- [138] Á. Imre, E. Gontier-Moya, D.L. beke, I.A. Szabó, G. Erdélyi, *Surf. Sci.* 441 (1999) 133.
- [139] K.F. McCarty, N.C. Bartelt, *Phys. Rev. Lett.* 90 (2003) 046104.
- [140] S. Kodambaka, V. Petrova, A. Vailionis, P. Desjardins, D.G. Cahill, I. Petrov, J.E. Greene, *Thin Solid Films* 392 (2001) 164.
- [141] S. Kodambaka, V. Petrova, S.V. Khare, D. Gall, A. Rockett, I. Petrov, J.E. Greene, *Phys. Rev. Lett.* 89 (2002) 176102.
- [142] S. Kodambaka, V. Petrova, A. Vailionis, I. Petrov, J.E. Greene, *Surf. Sci.* 526 (2003) 85.
- [143] S. Kodambaka, N. Israeli, J. Bareño, W. Świąch, K. Ohmori, I. Petrov, J.E. Greene, *Surf. Sci.* 560 (2004) 53.
- [144] W.-C. Yang, M. Zeman, H. Ade, R.J. Nemanich, *Phys. Rev. Lett.* 90 (2003) 136102.
- [145] Y. He, E. Borguet, *J. Phys. Chem. B* 105 (2001) 3981.
- [146] Y. He, E. Borguet, *Faraday Discuss.* 121 (2002) 1.
- [147] S. Dieluweit, M. Giesen, *J. Phys. Condens. Matter* 14 (2002) 4211.
- [148] S. Baier, S. Dieluweit, M. Giesen, *Surf. Sci.* 502–503 (2002) 463.
- [149] D.L. Chopp, *J. Comput. Phys.* 162 (2000) 104.
- [150] M. Giesen, G.S. Icking-Konert, *Surf. Sci.* 412–413 (1998) 645.
- [151] C.R. Stoldt, A.M. Cadilhe, C.J. Jenks, J.-M. Wen, J.W. Evans, P.A. Thiel, *Phys. Rev. Lett.* 81 (1998) 2950.
- [152] A.M. Cadilhe, C.R. Stoldt, C.J. Jenks, P.A. Thiel, J.W. Evans, *Phys. Rev. B* 61 (2000) 4910.
- [153] M. Eßer, K. Morgenstern, G. Rosenfeld, G. Comsa, *Surf. Sci.* 402–404 (1998) 341.
- [154] H. Shao, S. Liu, H. Metiu, *Phys. Rev. B* 51 (1995) 7827.
- [155] P. Jensen, N. Combe, H. Larralde, J.L. Barrat, C. Misbah, A. Pimpinelli, *Eur. Phys. J. B* 11 (1999) 497.
- [156] W.W. Pai, J.F. Wendelken, C.R. Stoldt, P.A. Thiel, J.W. Evans, D.-J. Liu, *Phys. Rev. Lett.* 86 (2001) 3088.
- [157] D.-J. Liu, J.W. Evans, *Phys. Rev. B* 66 (2002) 165407.
- [158] D.L. Chopp, J.A. Sethian, *Interfaces Free Bound.* 1 (1999) 1.
- [159] S. Kodambaka, D.L. Chopp, I. Petrov, J.E. Greene, *Surf. Sci. Lett.* 540 (2003) L611.
- [160] K. Arenhold, S. Surnev, P. Coenen, H.P. Bonzel, P. Wynblatt, *Surf. Sci.* 417 (1998) L1160.
- [161] C. Bombis, A. Emundts, M. Nowicki, H.P. Bonzel, *Surf. Sci.* 511 (2002) 83.
- [162] M. Nowicki, C. Bombis, A. Emundts, H.P. Bonzel, *Phys. Rev. B* 67 (2003) 075405.